RCTA
Revista Colombiana de Tecnologías de Avanzada
UNIPAMPLONA

Parametric analysis of EMAT spiral coils through multiphysics simulations in COMSOL

Análisis paramétrico de bobinas espirales EMAT mediante simulaciones multifísicas en COMSOL

Ing. Miguel Ángel Ríos Tarazona[1], **Dr. Jhon Jairo Padilla Aguilar**[2], **MSc. Sandra Johana Benítez Muñoz**[1], **Dr. Luis Ángel Silva**[3], **MSc. Juan Carlos Villamizar Rincón**[3], **Ing. Daniel Felipe Bernal Mejía**[2], **Dr. Mauricio Barrios Castellanos**[3]

[1] **Fundación Universitaria de San Gil,** IDENTUS, San Gil, Santander, Colombia.
[2] **Corporación para la Investigación de la Corrosión,** Tecnologías de Inspección, Piedecuesta, Santander, Colombia.
[3] **Universidad Pontificia Bolivariana,** Bisemic, Piedecuesta, Santander, Colombia.

Correspondence: investigadordit1.bga@upb.edu.co

Received: june 02, 2026. **Revised:** august 18, 2026. **Accepted:** september 07, 2026. **Published:** september 09, 2026.

How to cite: M. A. Ríos Tarazona, J. J. Padilla Aguilar, S. J. Benítez Muñoz, L. A. Silva, J. C. Villamizar Rincón, D. F. Bernal Mejía, and M. Barrios Castellanos, "Parametric analysis of EMAT spiral coils through multiphysics simulations in COMSOL", *Revista Colombiana de Tecnologías de Avanzada (RCTA)*, vol. 2, no. 48, pp. 236–250, sept. 2026, doi: 10.24054/rcta.v2i48.4522

Abstract: This work presents a parametric analysis of spiral-coil electromagnetic acoustic transducers (EMATs) using multiphysics simulations in COMSOL Multiphysics. The model integrates a spiral coil, a permanent magnet, and a conductive test plate, and is solved on a two-dimensional planar domain in which the cross-section of its conductors represents the spiral. The study evaluates the influence of excitation-signal parameters and coil and magnet geometry on the generation and propagation of ultrasonic waves in metallic plates. The campaign comprises ten parameters, each evaluated at six levels, using a one-factor-at-a-time design, with a common base condition at the midpoint of each interval. The results show that both the envelope coefficient of the excitation pulse and the amplitude of the applied current yield quantifiable variations in the response magnitude and duration. The magnet aspect ratios and the winding parameters modify the magnetic field distribution and, consequently, the simulated mechanical response. Variations of the carrier central frequency reveal a trade-off between signal amplitude and temporal resolution, which is decisive for defect detection. These findings provide practical guidelines for optimizing the design of spiral-coil EMATs, thereby improving signal quality and reliability in non-destructive testing applications.

Keywords: electromagnetic acoustic transducer, non-destructive testing, ultrasound, predictive maintenance, mechanical design.

Resumen: Este trabajo presenta un análisis paramétrico de transductores acústicos electromagnéticos (EMAT) de bobina en espiral mediante simulaciones multifísicas en COMSOL Multiphysics. El modelo integra una bobina en espiral, un imán permanente y una placa conductora de ensayo y se resuelve en un dominio bidimensional plano en el que la espiral se representa mediante la sección transversal de sus conductores. El estudio evalúa la influencia de los parámetros de la señal de excitación y de la geometría de la bobina y del imán sobre la generación y propagación de ondas ultrasónicas en placas metálicas. La campaña comprende diez parámetros evaluados en seis niveles cada uno, mediante un diseño de variación de un factor a la vez, con una condición base común situada en el punto medio de cada intervalo. Los resultados muestran que tanto el coeficiente de la envolvente del pulso de excitación como la amplitud de la corriente aplicada producen variaciones cuantificables en la magnitud y la duración de la respuesta. Las relaciones de aspecto del imán y los parámetros del devanado modifican la distribución del campo magnético y, en consecuencia, la respuesta mecánica simulada. Las variaciones de la frecuencia central de la portadora evidencian un compromiso entre la amplitud de la señal y la resolución temporal, lo cual resulta determinante para la detección de defectos. Estos hallazgos proporcionan lineamientos prácticos para optimizar el diseño de EMATs de bobina en espiral, lo que contribuye a mejorar la calidad de la señal y la confiabilidad en aplicaciones de ensayos no destructivos.

Palabras clave: transductor acústico electromagnético, ensayos no destructivos, ultrasonido, mantenimiento predictivo, diseño mecánico.

1. INTRODUCTION

Pipelines used in the oil and gas industry are critical components that require periodic inspections to guarantee their integrity and safety [1]. The presence of cracks or defects can cause leaks, catastrophic failures, and environmental risks, which makes effective inspection techniques indispensable [2]-[4].

Non-Destructive Testing (NDT) comprises a set of techniques used to evaluate the properties of a material or system without causing damage. These methodologies are widely used in various industrial sectors, especially in hydrocarbon transport, to detect discontinuities in pipelines. Among the most common techniques are visual inspection, ultrasound, radiography, magnetic particles, and penetrant liquids [5], [6]. At present, NDT enables improved efficiency in inspecting metallic components and enhanced operational reliability of facilities.

Among the different types of ultrasonic transducers used in industry, the electromagnetic acoustic transducer (EMAT) constitutes an alternative to conventional ultrasound. Unlike the conventional ultrasonic transducer, the EMAT requires no couplant to transmit waves into the material and can operate over a very wide temperature range [7], [8]. The EMAT system is composed mainly of a permanent magnet, an excitation coil, and a test sample. The coil generates a variable electromagnetic field that, upon interacting with the permanent magnet's magnetic field, produces Lorentz forces capable of inducing acoustic waves in the material.

These acoustic waves propagate through the part until they encounter a discontinuity or the material boundary, generating reflections that enable defect identification or thickness estimation [9]-[11]. The displacement amplitude conditions the attainable signal-to-noise ratio, and the time of flight conditions the thickness resolution [12].

The operation of the EMAT can be modeled using Lorentz forces in the COMSOL Multiphysics software, enabling optimization of its design and improved performance in detecting defects in metallic materials. In EMAT technology, various coil configurations are used to generate both longitudinal and shear waves. Among them, spiral coils are widely used for their directivity and for the focusing of the generated wave.

The design of a spiral-coil EMAT requires the simultaneous setting of electrical and geometric parameters. Yet, their effects on the signal's amplitude and time of flight are not documented jointly, so selection is not based on the signal's behavior but on transfer across different geometries. The available background addresses the problem only partially, as summarized in Table 1.

The literature reports alternative coil configurations aimed at specific wave modes. The directivity of the acoustic field of a butterfly coil was measured on a plate [13], combined with a multilayer coil with periodic permanent magnets to generate shear horizontal waves [14] and with a meander line coil to excite a single Lamb wave mode [15].

The magnet geometry also conditions the transducer's response. Du et al. [16] simulated by finite elements an EMAT with periodically arranged permanent magnets. The study evaluated the effect of the magnet parameters on the amplitude ratio between the Lamb wave modes. Strizhak and Pryakhin [17] optimized the mass and dimensions of the magnetizing device and reduced the transducer's weight.

The Lorentz force is not the only transduction mechanism. In ferromagnetic materials, magnetostriction also contributes to sound generation. Liang et al. report a magnetostrictive-based EMAT with a high magneto-acoustic transduction efficiency [18].

The separation between the coil and the part conditions the recorded amplitude. Xiang et al. experimentally characterized the effect of *lift-off* on the generation of surface acoustic waves [19].

The contribution of this work does not lie in simulating an EMAT by finite elements [7]-[11], but in evaluating ten parameters on a single model and under a common base condition, which makes it possible to compare the sensitivity of heterogeneous parameters (electrical, coil geometry, and magnet geometry) within the same simulation framework.

The objectives of this work are: (i) to formulate a two-dimensional planar multiphysics model of the coil-magnet-plate assembly that couples the electromagnetic problem with the mechanical one through the Lorentz force; (ii) to quantify the individual influence of the excitation-signal parameters and of the transducer geometry on the mechanical displacement and the von Mises stress; and (iii) to delimit the favourable conditions within the simulated intervals.

The analysis focuses on the amplitudes of the generated displacement and the echo at the analysis point. The planar geometry adopted does not account for directivity, so the directivity properties reported for spiral coils [5], [20] are cited as background rather than as the object of evaluation for this model.

This document is organized as follows: Section 2 presents the methodology, which covers the formulation of the multiphysics and geometric models, material properties, discretization, excitation signal, experimental design, metrics used, and model limitations. Section 3 presents the results and their corresponding discussion. Finally, Section 4 presents the study's conclusions.

***Table 1:** Comparison with the works used as background.*

Work	Which parameter varies	Conditions	Main result	Difference with this study
[8] **Zhai *et al.* (2017)**	Coil structure of a phased array	Metallic plate, sectorial scan	Coil design for sectorial imaging	Does not evaluate magnet aspect ratios or excitation-signal parameters
[9] **Guo *et al.* (2023)**	Coil *racetrack* with periodic permanent magnets	Selective generation of Lamb waves	Selective enhancement of one wave mode	Optimizes one specific mode, not the parametric sensitivity of the transducer
[11] **Wu *et al.* (2025)**	Coil geometry and detection circuit	EMAT without magnet, 304 stainless steel	Joint design of transducer and circuit	Does not evaluate the magnet geometry, absent from its configuration
This work	Ten parameters, six levels each	Planar model, steel plate, base condition at the midpoint of each interval	Individual sensitivity of each parameter under a common reference	Parametric coverage and base condition shared between families of parameters

***Source:** own elaboration.*

2. METHODOLOGY

2.1. Multiphysics formulation

The study established the input parameters based on results reported in previous research to ensure the validity of the simulations conducted.

The simulations were run in COMSOL *Multiphysics* using the electromagnetism module, governed by Maxwell's equations, and the structural mechanics module to evaluate the material's mechanical response.

The model was solved in COMSOL Multiphysics 6.2.0.415 (win64). The electromagnetic interface is *Magnetic Fields* (mf) with an out-of-plane vector-potential formulation, and the mechanical one is *Solid Mechanics* (solid) under a plane-strain approximation with unit thickness. Both are coupled through the multiphysics node *Magnetomechanics* (mmcpl1), which uses the AC/DC and MEMS modules. The study consists of two steps: a stationary step, which establishes the permanent magnet's polarization, and a time-dependent step, which solves for the propagation.

The equations that describe the behavior of the model are the following:

$$J = \sigma(E + v \times B) \quad (1)$$

This equation describes the current density induced in the material. The term σ represents the electrical conductivity, E the electric field, v the velocity of the particles, and B the magnetic flux density.

$$E = -\frac{\partial A}{\partial t} \quad (2)$$

The previous equation relates the electric field E to the magnetic vector potential. $\frac{\partial A}{\partial t}$ as a function of time.

$$\nabla \times H = J \quad (3)$$

This expression corresponds to Ampère's law, where H represents the magnetic field intensity and J the current density.

$$B = \nabla \times A \quad (4)$$

The equation defines the magnetic flux density B from the magnetic vector potential A.

$$J = \sigma E + \sigma v \times B + J_e \quad (5)$$

This relation incorporates the external current density J, corresponding to the excitation applied to the coil of the EMAT transducer.

$$\rho \frac{\partial^2 u}{\partial t^2} = \nabla \cdot (FS)^T + F_v \quad (6)$$

The previous equation describes the mechanical behavior of the material. The term ρ represents the density of the material, u the mechanical displacement; S, the stress tensor; and F, the volumetric force applied on the domain.

$$F_v = J \times B \quad (7)$$

This last equation corresponds to the Lorentz force and represents the model's electromechanical coupling. The interaction between the current density J and the magnetic field B generates forces on the test plate, which induce mechanical vibrations that propagate ultrasonic waves through the EMAT transducer.

2.2. Geometric modeling and representation of the coil

The EMAT model consists of three main components: the test plate, the spiral coil, shown in Figures 2 and 3, and the magnet, shown in Figure 4. Figure 1 presents the complete model.

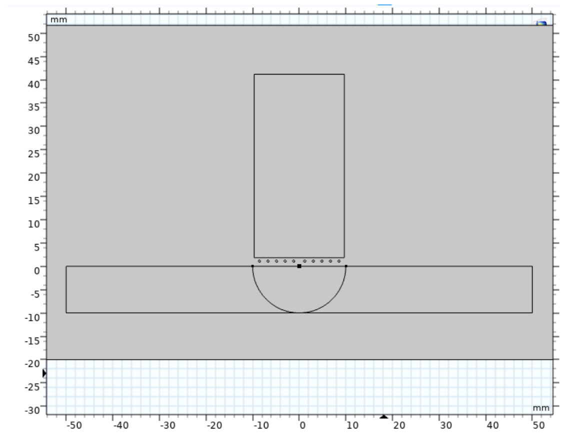

Fig. 1. *EMAT model in COMSOL Multiphysics*
Source: *own elaboration.*

This work analyses the internal and external diameters, the conductor diameter, and the spacing between turns. The *lift-off* distance between the coil and the test plate was also considered. The magnet geometry was evaluated through aspect ratios associated with its width and its height.

The model is solved on a two-dimensional planar domain, under a plane-strain approximation and with unit out-of-plane thickness. The electromagnetic interface solves the out-of-plane vector potential, and the geometry is built by mirroring the winding about the central plane, so that the complete cross-section is computed. Consequently, the spiral coil is not represented as a planar spiral nor as a set of circular turns. Each circle in Figures 2 and 3 corresponds to the cross-section of a straight conductor, and the two groups of ten are the outgoing and returning branches of the winding.

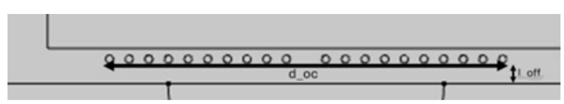

Fig. 2. *Model of the EMAT coil in COMSOL Multiphysics. Each circle represents the cross-section of a straight conductor of the winding; the domain is planar, not axisymmetric.*
Source: *own elaboration.*

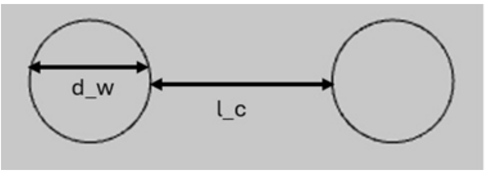

***Fig. 3**. Close-up of the EMAT coil model in COMSOL Multiphysics, with the separation between conductors l_c and the conductor diameter d_w that define the ratio k_{lc}.*
***Source:** own elaboration.*

This simplification delimits the scope of the results. The model represents the cross-section of the coil-magnet-plate assembly and reproduces neither the spiral pitch nor the winding closure. The field distribution obtained corresponds to the cutting plane, so that the effects outside that plane are excluded, and the model does not support claims about radial focusing towards an axis nor about azimuthal directivity, because neither of the two is represented in the resolved geometry. What it does allow to evaluate, and what is reported, are the displacement amplitude and the time of flight at the analysis point.

In Figure 1, in addition to the main components, an analysis point is shown, used to evaluate the von Mises stress, displacement, magnetic flux density, and current density locally. This point enabled analysis of the spatial variations in the physical variables considered in the study.

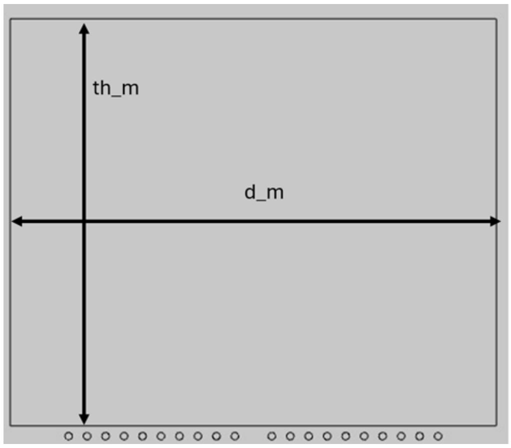

***Fig. 4**. Model of the magnet in COMSOL Multiphysics, with the width d_m and the height th_m that define the aspect ratios k_{m1} and k_{m2}. **Source:** own elaboration.*

2.3. Material properties

The physical parameters of the materials were the following: for the steel, an electrical conductivity of 4.032×10^6 S/m, a relative magnetic permeability of 1, and a density of 7 850 kg/m^3. For the air, an electrical conductivity of 0 S/m, a relative magnetic permeability of 1, and a density of 1.225 kg/m^3 were considered. For the copper, an electrical conductivity of 5.998×10^7 S/m, a relative magnetic permeability of 1, and a density of 8 960 kg/m^3.

The computational model developed considers that the effects of magnetostriction are minimal compared with those of the Lorentz force. Therefore, the Lorentz force is the only multiphysics coupling mechanism represented. This is consistent with the system of equations (1)-(7), in which no magnetostrictive term appears, and delimits the scope of the results, which are not extrapolable to materials in which magnetostriction contributes appreciably to acoustic generation [18].

The magnet is sintered NdFeB N50, with remanence $B_r = 1.41$ T, recoil permeability of 1.05 and conductivity of 7.14×10^5 S/m; its orientation is defined by specifying the north and south faces.

2.4. Discretization

To improve the numerical behavior of the simulations, the geometry was discretized with three mesh levels. The finest mesh was applied on the test plate and on the coil, since these regions present the largest field gradients. The coarsest mesh was used in the air domain, where no significant induced currents are generated. Finally, an intermediate mesh was used on the magnet.

The mesh sizes were selected with the aim of reducing the simulation time without compromising the accuracy of the results. Figure 5 shows the difference between the meshes used.

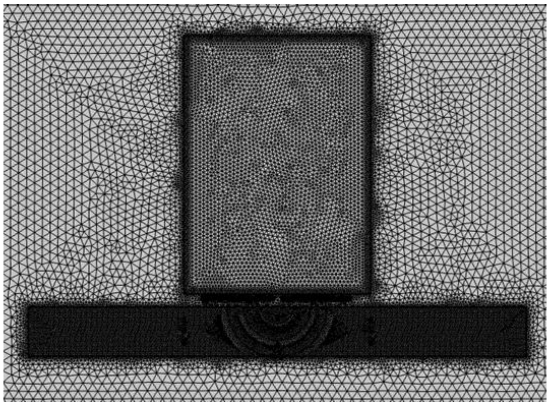

***Fig. 5**. Mesh of the geometry of the EMAT model*
***Source:** own elaboration.*

The fine mesh was built with custom aspect-ratio parameters, with the aim of adequately representing the regions of high field gradient. The maximum element size was set to 0.4 mm and the minimum to 0.001 mm.

RCTA
Revista Colombiana de Tecnologías de Avanzada
UNIPAMPLONA

The maximum element growth rate was set to 2, which guarantees a gradual transition between refined regions and regions of larger element size. The curvature factor was set to 0 and 2, which allowed additional refinement on curved surfaces. Finally, the resolution in narrow regions was set to 0.4, which improved the representation of thin layers and of regions affected by the skin effect.

The coarse mesh was generated with custom size parameters to reduce the computational cost in the regions of lower electromagnetic interest. The maximum element size was set to 2 mm and the minimum to 0.001 mm.

The maximum growth rate was set to 2, while the curvature factor was set to 0.2. The resolution in narrow regions was set to 0.4, which guarantees an adequate geometric representation without excessively increasing the number of elements.

The intermediate mesh applied to the magnet used a maximum element size of 1 mm and a minimum size of 0.001 mm. The maximum growth rate was set to 1.3, which allows a smooth transition between the refined regions and those of lower resolution.

The curvature factor was set to 0.3, while the resolution in narrow regions was set to 1. This configuration made it possible to represent the geometry of the magnet adequately without generating an excessive number of elements.

Figure 6 compares the displacement magnitude field obtained with two different discretizations of the internal domain. The values used for the discretization of Figure 6a were: maximum element size of 2 mm, minimum size of 0.25 mm, maximum growth rate of 2, and curvature factor of 0.2. The parameters in Figure 6b correspond to those previously described for the study model. Both maps share the same color scale, from 3.05×10^{-16} m to 1.3×10^{-10} m, so that the appreciable differences are concentrated in the wavefront texture rather than in the maximum field value.

The resulting mesh consists of 53 676 triangular elements and 26 964 vertices, with a minimum quality of 0.0124 and a mean quality of 0.8743 over an area of 15 450 mm^2. The discretized problem has 175 398 degrees of freedom. These figures describe the discretization used but do not constitute a convergence study: the model was solved with a single mesh, so the uncertainty associated with the element size is unbounded.

The parameters of the mesh shown in Figure 6b correspond to those previously defined for the model used in the study.

Finally, the analysis evaluated the individual influence of each variable on the response of the system through independent simulations.

To validate the computational model, the results obtained were contrasted with the trends reported in the literature [8], [9], [11]. The referenced works indicate that parameters such as the lift-off, the induced current, and the magnet geometry produce quantifiable variations in the behavior of the system, in agreement with the trends observed in the present study.

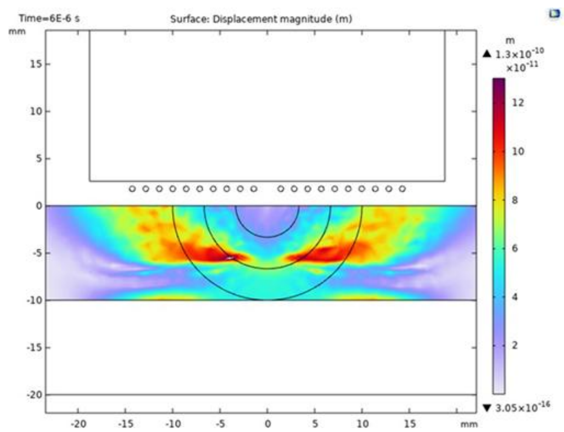

(a) Coarser mesh

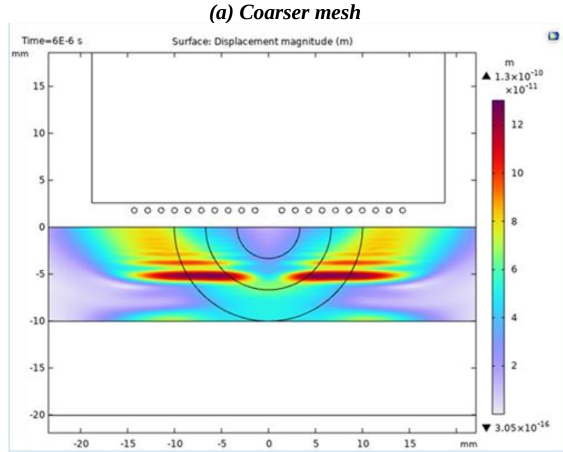

(b) Mesh used in the study

***Fig. 6**. Displacement magnitude field at t = 6 µs obtained with (a) a coarser discretization and (b) the discretization used in the study. Both maps share the same color scale. The mesh itself is shown in Figure 5. **Source:** own elaboration.*

2.5. Modeling of the excitation signal

The excitation signal used in the simulations is defined through a function known as a Gabor pulse or *tone burst* with a Gaussian envelope, whose mathematical expression is:

$$y(t) = \beta\, e^{\{-\alpha_f (t - \tau)^2\}} \cos(2\pi\, f_0\, (t - \tau)) \quad (8)$$

where β represents the maximum amplitude of the current [A], α_f is the Gaussian decay factor that controls the temporal width of the pulse, f_0 is the central frequency of the carrier [Hz], and τ is the temporal delay that shifts the center of the pulse with respect to the origin [s]. This formulation combines a Gaussian envelope, which confines the energy of the pulse to a finite time interval, with a cosine oscillation at the operating frequency of the EMAT transducer, which guarantees a spectral content concentrated around. f_0.

Figure 7 illustrates the behavior of this signal in a base configuration defined by β = 300 A, f_0 = 2 MHz, α = 4 and τ = 4 µs, varying the parameters of the signal.

Figure 7 illustrates the individual variations of each parameter: first, the amplitude was increased to β = 400 A while keeping the remaining values constant, then the frequency was changed to f_0 = 4 MHz and, finally, the decay factor α_f was varied, showing the isolated influence of each parameter on the waveform.

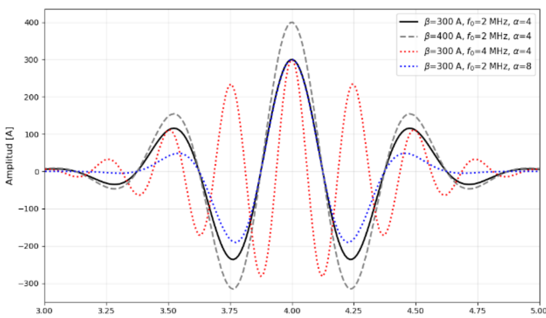

***Fig. 7**. Input signal of the simulation. The curves were generated with rounded values for illustrative purposes (β = 300 A, f_0 = 2 MHz, α_f = 4, τ = 4 µs) and do not reproduce the base condition of Table 2: their purpose is to show the isolated effect of each term of the Gabor pulse on the waveform, not to represent a simulation of the parametric campaign.*
***Source:** own elaboration.*

The transient study runs from 0 to 12 µs with an output step of 0.1 µs, that is, 121 instants. The integrator is of the *Generalized-alpha* type with an adaptive internal step, a relative tolerance of 0.001 and an absolute tolerance per field of 0.1; the initial internal step is 1.2 × 10^{-8} s. The nonlinear geometry is activated. Each simulation requires 48 s of computation.

2.6. Experimental design, base condition and variation ranges

The study used a one-factor-at-a-time methodology (*One-Factor-at-a-Time*, OFAT), in which each parameter was modified individually, while the others remained constant at a reference value. This approach made it possible to evaluate in isolation the direct influence of each variable on the response of the transducer. The parameters to be analyzed are presented in Table 2.

***Table 2:** Input parameters of the EMAT model*

Parameter	Value	Description
β	305 A	Signal amplitude.
f_0	2.25 MHz	Central frequency of the signal.
α_f	5.2	Envelope coefficient of the signal.
k_{lc}	1.5	Ratio between the separation of conductors and their diameter.
k_{m1}	1.25	Ratio between the magnet width and the coil diameter.
k_{m2}	1.65	Ratio between the magnet height and its width.
d_w	0.57 mm	Conductor diameter.
k_{dic}	2.5	Ratio between the internal coil diameter and the conductor diameter.
l_{off}	1.5 mm	Separation between the test plate and the coil (*lift-off*).
d_{oc}	30 mm	External diameter of the coil.

***Source:** own elaboration*

The analysis included a total of 60 simulations. This number is obtained by multiplying the ten parameters evaluated at the six levels defined for each parameter, according to Table 3. The simulations were carried out in COMSOL *Multiphysics* according to the specifications previously described.

***Table 3:** Variation levels of the evaluated parameters*

β [A]	10.00	128.00	246.00	364.00	482.00	600.00
f_0 [MHz]	0.50	1.20	1.90	2.60	3.30	4.00
α_f	0.50	2.40	4.30	6.20	8.10	10.00
k_{lc}	0.00	0.60	1.20	1.80	2.40	3.00
k_{m1}	0.50	0.80	1.10	1.40	1.70	2.00
k_{m2}	0.30	0.84	1.38	1.92	2.46	3.00
d_w [mm]	0.15	0.32	0.49	0.66	0.83	1.00
k_{dic}	1.00	1.60	2.20	2.80	3.40	4.00
l_{off} [mm]	0.00	0.60	1.20	1.80	2.40	3.00
d_{oc} [mm]	12.00	19.00	26.00	34.00	41.00	48.00

The coil diameter and the aspect ratios of the permanent magnet reproduce the values reported in designs with narrow and wide magnets [3], [20]. The conductor diameter corresponds to the gauges used in EMAT windings [14]. The external diameter of the coil coincides with the values used in plate inspection with a spiral coil [8]. The *lift-off* interval corresponds to the one characterized experimentally [19], and its null level constitutes a limiting case, not an operating condition. The ratio between the coil diameter and the conductor diameter is exploratory and assesses the sensitivity of the internal coil diameter.

The parameter k_{lc} represents the ratio between the separation of conductors l_c and their diameter d_w:

$$k_{lc} = \frac{l_c}{d_w} \qquad (9)$$

The parameter k_{m1} defines the ratio between the magnet width d_m and the coil diameter d_{oc}, and the parameter k_{m2} the ratio between the magnet height th_m and its width:

$$k_{m1} = \frac{d_m}{d_{oc}} \qquad (10)$$

$$k_{m2} = \frac{th_m}{d_m} \qquad (11)$$

The parameter k_{dic} represents the ratio between the internal coil diameter and the conductor diameter, and l_{off} corresponds to the separation between the test plate and the coil.

The decay factor of the input signal is given by

$$\alpha = \alpha_f f_0^2 \qquad (12)$$

which is not independent of the frequency. The envelope of the pulse narrows with the square of the frequency, while the number of cycles contained in it remains constant. The sweep of f_0 therefore modifies the carrier and the envelope at the same time, and its results must not be interpreted as the isolated effect of the frequency.

The values in Table 2 were adopted as the model's base conditions, which correspond to those used in the simulation campaign. These values were built through an explicit rule: each one is the midpoint of the interval swept for that parameter, that is, the mean of the two central levels of Table 3.

The six levels of each parameter are uniformly spaced between the minimum and the maximum of the interval. The conclusions derived from this sweep are strictly valid within the simulated intervals; neither linearity, nor proportionality, nor extrapolability outside the studied domain is assumed.

Each effect reported in Section 3 corresponds to a marginal effect evaluated at the base condition of Table 2. The one-factor-at-a-time design makes it possible to isolate the individual influence of each variable under controlled conditions. Still, it does not make it possible to estimate the interactions between parameters.

Two couplings are foreseeable from the definitions themselves: k_{m1} and k_{m2} share the magnet width d_m (Equations (10) and (11)). Therefore, they are geometrically dependent on each other, and k_{m1} relates the magnet to the coil diameter d_{oc}, so that the geometry of the magnet and that of the coil are not separable either. Estimating these interactions requires a factorial or response-surface design, which is proposed for future work.

The study establishes a hierarchy between the output variables to facilitate the interpretation of the observed phenomena. The mechanical displacement constitutes the main indicator of the acoustic performance of the transducer, since it directly reflects the generation and the magnitude of the ultrasonic wave propagated in the material. The von Mises stress, the magnetic flux density and the current density are considered complementary variables, which make it possible to interpret the underlying physical mechanism and show how the electromagnetic interaction and the resulting Lorentz force are transformed into an observable mechanical response.

The literature reports a positive correlation between the von Mises stress and the magnetic field density [8], [11]. It is not a general physical proportionality relation: the Lorentz force of Equation (7) is the product $J \times B$, so that proportionality with B can only be sustained when J remains constant, a condition that is not met when the coil geometry is modified. In this work, the relation is expressed as a correlation observed under the simulated conditions.

2.7. Metrics and extraction procedure

All the metrics are extracted from the signal recorded at the analysis point on the lower face of the plate, along the axis of the winding. The record is divided into two windows:

- The **emission** one, $t < 8$ μs, which collects the direct excitation, and
- The **echo** one, $t > 8$ μs, which collects the signal reflected on the opposite face.

The displacement is negative throughout the record because of the reference system's orientation, so it is analyzed in absolute value.

The **time of flight** is the instant of the local extremum that marks the arrival of the echo within its window, measured from the origin of the record:

$$t_x = t|_{\min(|u|),\ t>8\ \mu s} \qquad (13)$$

and analogously for the von Mises stress, whose echo is marked by a maximum:

$$t_\sigma = t|_{\max(\sigma),\ t>8\ \mu s} \qquad (14)$$

The amplitude of each signal is its root mean square value in the echo window, over the N instants that compose it. It is a stable magnitude, which does not depend on which of the oscillations turns out to be the largest:

$$A_x = \sqrt{\frac{1}{N}\sum_k |u_k|^2}, \qquad A_\sigma = \sqrt{\frac{1}{N}\sum_k \sigma_k^2} \qquad (15)$$

The normalized amplitude compares the six levels of the same parameter. It is defined as the quotient between the amplitude of each level and the largest of the six, so that it equals 1 at the level of greatest amplitude:

$$x_{norm} = \frac{A_{x,i}}{\max_i(A_{x,i})}, \qquad \sigma_{norm} = \frac{A_{\sigma,i}}{\max_i(A_{\sigma,i})} \quad (16)$$

The definition of the time of flight admits an independent physical check. The analysis point is on the lower face of a 10 mm plate, and the pulse carries a delay $\tau = 4$ μs. With $E \approx 200$ GPa, $\nu \approx 0.33$ and $\rho = 7850$ kg/m³, the shear-wave velocity is 3095 m/s, so that a 20 mm round trip places the echo at 10.46 μs. This is the value of 10.4 μs that appears in Figures 11 to 13 and, until now, has been cited as an expected value without justification. Table 4 presents the metrics used for each analyzed variable.

Table 4: *Metrics used in the analysis of results.*

Metric	Definition	Unit	Window
t_x, t_σ	Equations (13) and (14)	μs	Echo, $t >$ 8 μs
A_x, A_σ	Equation (15), root-mean-square value	m and Pa	Echo, $t >$ 8 μs
x_{norm}, σ_{norm}	Equation (16)	dimensionless	Six levels of a parameter
Envelope width	$2\sqrt{\ln 2/\alpha}$, full width at half maximum	μs	Excitation signal

Source: *own elaboration. All are extracted at the analysis point of Figure 1.*

2.8. Limitations of the model

The model was solved using a single discretization; no quantitative convergence study is available, so the uncertainty associated with the element size is unbounded.

The study uses a *Generalized-alpha* integrator with a relative tolerance of 0.001 and an output step of 0.1 μs over 12 μs of simulation. These settings are documented in Section 2.5 but were not subjected to a sensitivity analysis, so no numerical accuracy is demonstrated for the model in this respect.

The steel is modeled with unit relative permeability, and the coupling restricts the transduction to the Lorentz force. The validity of the results is limited to materials in which magnetostriction does not contribute appreciably.

Sections of straight conductors represent the spiral coil in a planar domain, which prevents resolving the effects outside the cutting plane and, in particular, the directivity of the beam. The mechanical boundaries are free, with no absorbing condition, so that the reflections at the edges of the 100 × 10 mm plate form part of the recorded signal.

The OFAT scheme does not estimate interactions between parameters. The study is exclusively computational. The trends obtained describe the model's behavior under the adopted assumptions and do not, on their own, constitute evidence of the performance of a physical inspection system; their transfer to practice requires subsequent experimental validation.

3. RESULTS AND DISCUSSION

3.1. Variation of the excitation-signal parameters

Table 5 summarizes the variation in the two output magnitudes between the first and last levels of each parameter, computed using the metrics in Section 2.7. It is the quantitative basis of the trends described below.

RCTA
Revista Colombiana de Tecnologías de Avanzada
UNIPAMPLONA

The results are presented as a function of the variation observed in each factor evaluated during the simulations. The first parameter analyzed was α_f, which determines the behavior of the transmitted signal. As the value of this factor increases, the amplitude of the recorded signal increases, accompanied by a decrease in the dispersion of the response.

***Table 5:** Variation of the echo amplitude between the first and the last level of each parameter.*

Parameter	Range	Displacement amplitude	von Mises stress
α_f	0.5 to 10	−98.8 %	−97.7 %
β	10 to 600 A	+4353 %	+6982 %
f_0	0.5 to 4 MHz	−89.7 %	−95.0 %
k_{m1}	0.5 to 2	−53.6 %	−39.6 %
k_{m2}	0.3 to 3	+338.0 %	+106.8 %
k_{lc}	0 to 3	−69.9 %	−77.3 %
d_w	0.15 to 1 mm	−49.8 %	−87.0 %
k_{dic}	1 to 4	+15.9 %	−8.6 %
l_{off}	0 to 3 mm	−42.1 %	−93.8 %
d_{oc}	12 to 48 mm	+85.6 %	−11.8 %

***Source:** own elaboration.*

This behavior favors the identification of the reflected signal, since a greater amplitude and a smaller dispersion of the peaks make it possible to distinguish the phenomena associated with the reflection. Figure 8 shows the signal obtained for different values of α_f.

Figure 8 excludes the signal for α_f = 0, whose high amplitude hinders the visualization of the remaining signals. A value of α_f = 0 suppresses the envelope coefficient, which produces a high-amplitude sinusoidal signal.

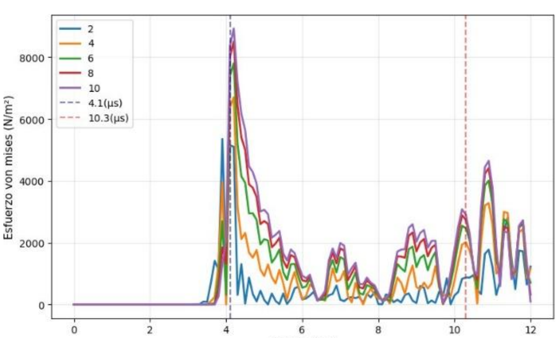

***Fig. 8**. Signal obtained for different values of α_f.*
***Source:** own elaboration.*

Figure 9 directly compares the signals corresponding to each value of α_f through a color map. The results confirm that a higher value of this parameter reduces the echo amplitude: between α_f = 0.5 and α_f = 10, the displacement amplitude falls by 98.8%, and that of the von Mises stress by 97.7 %.

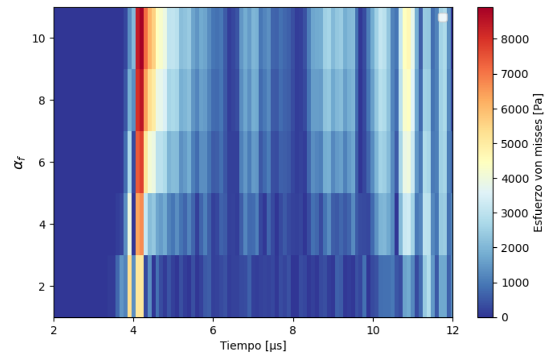

***Fig. 9**. Comparison of amplitudes for different values of α_f.*
***Source:** own elaboration.*

These results indicate that the level of the envelope coefficient determines the quality of the signal obtained and, consequently, the accuracy of the analysis.

In the case of the central frequency (f_0), as the frequency increases, the amplitude of the signal decreases, and the temporal width is reduced, which improves the temporal resolution, although at the cost of a lower intensity.

Figure 10 shows the signal obtained for different values of f_0. Increasing the parameter produces signals of smaller temporal width and lower amplitude. The color map confirms that high values of f_0 generate greater accuracy in the location of the reflected signal, although they reduce its magnitude.

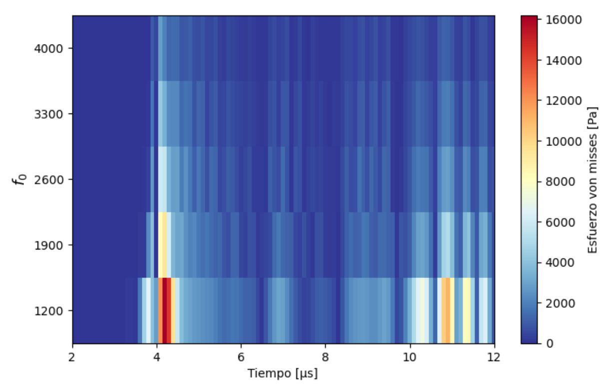

***Fig. 10**. Signal obtained for different values of f_0.*
***Source:** own elaboration.*

The simulations of f_0 also make it possible to evaluate the magnetic field density and the current density. The analysis of these variables records only the emission of the signal. The increase of f_0 produces a narrowing of the amplitude of the emitted signal.

The parameter β represents the amplitude of the excitation of the signal. As β increases, the amplitude of the recorded signal increases, which improves the visibility of the response of the material. The shape of the signal does not present appreciable variations, which indicates that β does not alter the nature of the response, but only its intensity. The increase of β is not always feasible in practice, since high currents can damage the equipment.

3.2. Magnet geometry

The influence of the geometric parameters of the magnet is analyzed as a function of two parameters of the simulation: the time of flight and the normalized amplitude.

The aspect ratio between the magnet width and the coil diameter (k_{m1}) modifies the response of the model: as the amplitude of the displacement signal increases k_{m1} the amplitude of the displacement signal decreases, and the von Mises stress also decreases, which indicates a lower intensity of the mechanical response. Figure 11 shows that the time of flight tends towards values below the expected value of 10.4 µs for ratios k_{m1} smaller than 1.4, despite presenting greater amplitudes, which indicates an inverse relation between resolution and signal intensity within the evaluated range

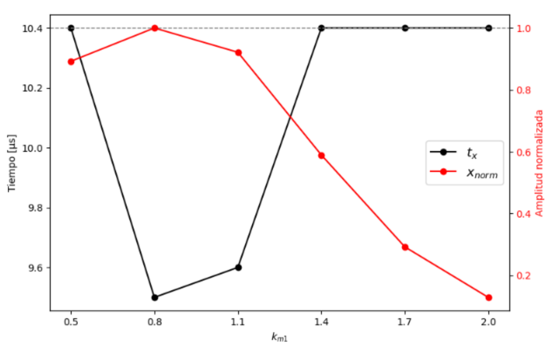

Fig. 11. *Variation of the time of flight and amplitude in mechanical displacement (x) as a function of the parameter* k_{m1}. *Left axis in microseconds; right axis dimensionless (normalized amplitude, Equations 15 and 16).*
Source: *own elaboration.*

On increasing k_{m2} the aspect ratio parameter between the magnet width and its height: the amplitude of the signal increases. Figure 12 shows that this increase presents an asymptotic behavior, where the gain in amplitude decreases as k_{m2} increases.

The aspect ratio of the magnet determines the amplitude of the generated signal, with an asymptotic effect that limits the gain beyond certain values of k_{m2}. High values of k_{m2} can generate practical difficulties in handling the equipment.

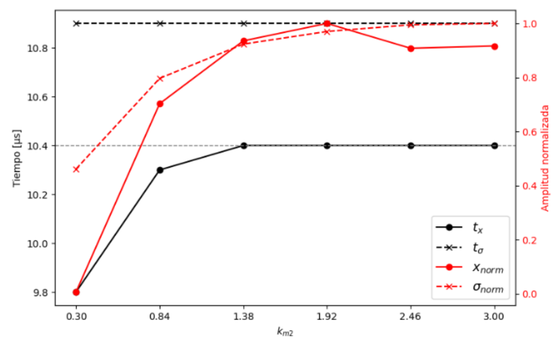

Fig. 12. *Variation of the time of flight and amplitude in mechanical displacement (x), the von Mises stress (σ) as a function of the parameter* k_{m2}. *Left axis in microseconds; right axis dimensionless.*
Source: *own elaboration.*

3.3. Coil geometry

The parameter k_{lc} represents the ratio between the separation between conductors and the conductor diameter. On increasing k_{lc} the amplitude of the signal decreases, which indicates that a greater separation between the conductors reduces the intensity of the generated signal. A smaller separation between conductors produces higher signals in the model. A reduced separation can generate difficulties in manufacturing.

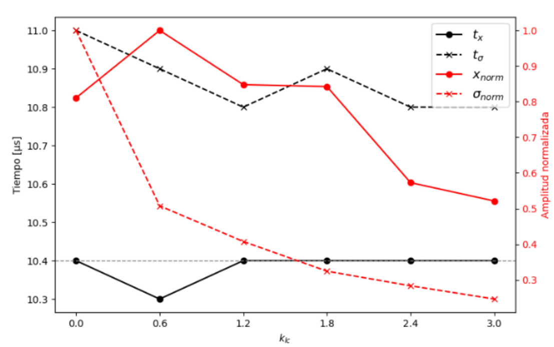

Fig. 13. *Variation of the time of flight and amplitude in mechanical displacement (x), the von Mises stress (σ) as a function of the parameter* k_{lc}. *Left axis in microseconds; right axis dimensionless.* ***Source:*** *own elaboration.*

The parameter d_w corresponds to the conductor diameter. On increasing d_w the amplitude of the displacement and of the von Mises stress decreases

(Figure 14). This reduction is due to the decrease in the number of turns of the coil, which reduces the current flowing through it. The increase of d_w increases the distance with respect to the magnet, which reduces the magnetic field density and the amplitude of the signal. This is an example of a variable that does not change in isolation: modifying d_w indirectly alters the number of turns of the winding.

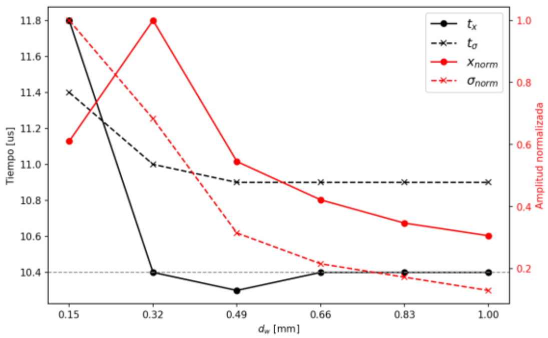

Fig. 14. *Variation of the time of flight and of the normalized amplitude as a function of the conductor diameter* d_w.
Source: *own elaboration.*

As observed in Figure 15, the analysis of the magnetic field shows that the offset of the signal varies only when the size of the magnet is modified or when the distance to the magnet is increased.

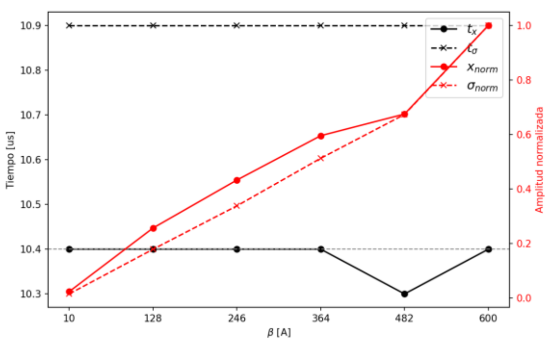

Fig. 15. *Variation of the time of flight and of the normalized amplitude as a function of the excitation amplitude* β.
Source: *own elaboration.*

Table 6 presents the variation of the polarization field at the analysis point and its Pearson correlation with the amplitude of the von Mises stress. The parameters that modify the magnet geometry or the assembly's distances from the plate show a positive correlation. In the remaining four, the field stays constant, and the correlation is undefined, even though the amplitude changes by orders of magnitude.

Table 6: *Variation of the polarization field at the analysis point and its correlation with the stress amplitude.*

Parameter	Variation of *B* [%]	*r*(*B*, σ)
k_{m2}	71.7	0.998
d_{oc}	38.9	0.768
k_{m1}	38.8	0.972
l_{off}	15.0	0.757
d_w	4.0	0.920
k_{lc}	0.2	—
f_0	0.02	—
β	0.00	—
k_{dic}	0.00	—

Source: *own elaboration.*

The von Mises stress is proportional to the magnetic field density when the latter varies. When the field is kept constant, the amplitude varies as a function of the applied current.

In the case of the lift-off parameter (Figure 16), the results show that a smaller separation between the plate and the coil favors the electromagnetic interaction, which increases the efficiency in the generation of the mechanical response and improves the performance of the transducer. This trend agrees qualitatively with the experimental characterization reported in [12]; the conditions of that work are not directly equivalent to those of this model, so that such agreement does not constitute a quantitative validation.

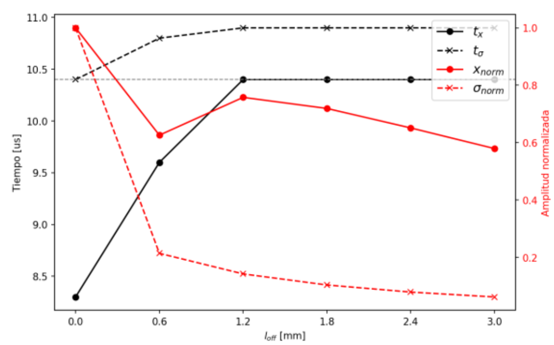

Fig. 16. *Variation of the time of flight and of the normalized amplitude as a function of the lift-off* l_{off}.
Source: *own elaboration.*

The parameter d_{oc} (Figure 17) presents a more favorable behavior in the range from 12 to 19 mm, since in that interval the current distribution and the interaction of the induced magnetic field reach an adequate balance. The maximum displacement amplitude at the analysis point within the simulated range is used as the favourability criterion.

RCTA
Revista Colombiana de Tecnologías de Avanzada
UNIPAMPLONA

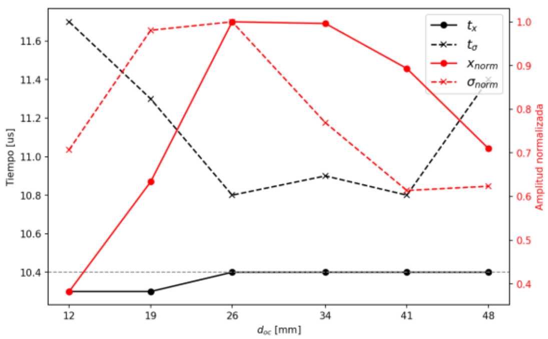

Fig. 17*. Variation of the time of flight and of the normalized amplitude as a function of the coil diameter* d_{oc}.
Source: *own elaboration.*

The analysis of the parameter k_{dic} did not show quantifiable changes in the global response of the system within the evaluated range, which indicates a low sensitivity of this variable with respect to the remaining conditions of the model.

3.4. Sensitivity synthesis

Table 7 ranks the ten parameters by the range of the normalized echo amplitude within their respective intervals and indicates the most favorable level for each one according to the criterion stated in Section 2.6: the maximum displacement amplitude at the analysis point. This table shows a hierarchy of marginal effects evaluated at the base condition, not a joint optimal configuration. Several of the favorable levels are at the extremes of the evaluated interval, indicating a design direction. The low sensitivity of k_{dic}, with a range of 0.137 compared to values above 0.6 for the rest, quantitatively confirms its low influence.

Table 7: *Sensitivity of each parameter and of the most favorable level within the simulated interval.*

Parameter	**Normalized amplitude range**	**Favourable level**	**Sensitivity**
α_f	0.997	0.5	high
β	0.978	600 A	high
f_0	0.897	0.5 MHz	high
k_{m2}	0.781	1.92	high
k_{lc}	0.699	0	high
d_w	0.694	0.32 mm	high
d_{oc}	0.617	26 mm	high
k_{m1}	0.613	0.80	high
l_{off}	0.421	0 mm	medium
k_{dic}	0.137	4	low

Source: *own elaboration.*

As the lift-off increases from 0 to 3 mm, the echo amplitude decreases by 42.1%, with a trend of the same sign as observed in the experimental characterization of [12]. When sweeping the central frequency from 0.5 to 4 MHz, the amplitude decreases by 89.7%, consistent with the amplitude-resolution trade-off described in [8] and [9]. And going from k_{m1} = 0.5 to 2, the amplitude falls by 53.6%, with the same sign as the enhancement by magnet geometry reported in [9]. The conditions of those works (material, thickness, wave type, and frequency) are not equivalent to those of this model, so the agreement is in trend and not in value. Table 8 summarizes these results.

Table 8: *Own magnitudes comparable with the literature.*

Compared magnitude	**Result of this work**	**Reference**
Amplitude against *lift-off*, from 0 to 3 mm	42.1 % drop	[12]
Amplitude against f_0, from 0.5 to 4 MHz	89.7 % drop	[8], [9]
Amplitude against k_{m1}, from 0.5 to 2	53.6 % drop	[9]

Source: *own elaboration. The conditions of the references - material, thickness, wave type, and frequency- are not equivalent to those of the model, so that the comparison is one of trend and not of value.*

4. CONCLUSIONS

The results obtained from the simulations show that the decay factor α_f produces variations in signal quality; its increase reduces dispersion and improves the resolution of the reflected signal, facilitating the identification of phenomena associated with the reflection. The central frequency f_0 determines the temporal resolution: higher values generate signals of smaller temporal width, although with a decrease in amplitude, which establishes a trade-off between resolution and signal energy.

The parameter β determines the magnitude of the signal without altering its shape, which improves the visibility of the response of the material. Nevertheless, the equipment imposes practical restrictions on its implementation, in particular because of the high current levels.

The aspect ratios k_{m1} and k_{m2} produce variations in the amplitude of the signal and in the measurement of the time of flight, which indicates the need to select the dimensions of the magnet according to the trade-off between amplitude and time of flight, since these determine the displacement and the intensity of the response.

The coil configuration parameters k_{lc} and d_w produce quantifiable effects on the response of the model, while k_{dic} shows low sensitivity in the evaluated range.

Within the evaluated conditions, a positive correlation is observed between the von Mises stress and the magnetic field density, linking the electromagnetic response to the material's mechanical behavior in the model, without this implying a general proportionality.

The results indicate that the response of the system depends on the balance between the analyzed parameters, since the individual adjustment of any of them can negatively affect the others. The selection of these parameters requires an integral analysis in order to guide the design within the scope of the model.

Quantitatively, the parameters that most strongly influence the echo amplitude are the envelope coefficient, the excitation amplitude, and the central frequency, with normalized amplitude ranges of 0.997, 0.978, and 0.897, respectively. The one with the least influence is the ratio between the internal coil diameter and the conductor diameter, at 0.137, four times lower than the next parameter. Among the geometric variables of the magnet and of the winding, the aspect ratio k_{m2} and the separation between conductors k_{lc} present ranges of 0.781 and 0.699. These figures correspond to marginal effects evaluated at the base condition of Table 2 and are valid within the intervals of Table 3.

This study is exclusively computational. Its conclusions describe the model's behavior under the adopted assumptions and are strictly valid within the simulated intervals in Table 3. The OFAT design does not estimate interactions between parameters. The spiral coil is represented by sections of straight conductors in a planar domain, thereby excluding from the analysis the effects outside the cutting plane and the beam's directivity. The work does not include experimental validation, so transferring these trends to a physical inspection system requires additional measurements.

As future work, the study proposes to implement statistical methodologies, such as factorial design of experiments (DoE) or response surface methods (RSM), that make it possible to quantify the interactions between the simulation parameters, as well as the experimental validation of the model on an instrumented plate.

Acknowledgments: The research was funded by the National Fund for Science, Technology and Innovation Financing, Francisco José de Caldas Fund, through contingent recovery financing contract No. 112721-400-2023.

REFERENCES

[1] Z. Wang y T. Pan, “Simulation study of continuous casting shell defect detection based on EMAT,” en *Proc. 39th Chinese Control Conf. (CCC)*, 2020, doi: 10.23919/CCC50068.2020.9188624.

[2] Y. Zhao, S. Wang, Y. Wang, H. Li y S. Huang, “Hybrid 2D-3D modeling method for electromagnetic acoustic phased array,” in *Proc. IEEE Int. Conf. Electronic Measurement & Instruments (ICEMI)*, 2023, doi: 10.1109/ICEMI59194.2023.10270395.

[3] J. Liu, S. Liu, C. Zhang, L. Jin y G. Zhao, “A new focused EMAT design with narrow magnet to achieve both A0-Lamb signal enhancement and waveform distortion correction,” *IEEE Sensors Journal*, vol. 22, 2022, pp. 14786–14798, doi: 10.1109/JSEN.2022.3185616.

[4] J. Wu y C. Wang, “Simulation analysis of EMAT shear wave in pipeline and research of defect detection characteristics,” in *Proc. Int. Conf. Intelligent Control, Measurement and Signal Processing (ICMSP)*, 2021, pp. 129–133, doi: 10.1109/ICMSP53480.2021.9513224.

[5] S.-J. Wang, Z.-J. Ma, Y.-Q. Li y Z.-Y. Qu, “3-D simulation for the acoustic field directivity of SH-wave EMATs,” en *Proc. Far East NDT New Technology & Application Forum (FENDT)*, 2017, doi: 10.1109/FENDT.2017.8584597.

[6] T. Zhang, X. Yang, M. Li, H. Peng y W. Peng, “Enhancing unilateral EMAT performance through topological optimization of Halbach permanent magnet arrays,” *NDT & E International*, 2024, art. no., doi: 10.1016/j.ndteint.2024.103172.

[7] S. Thomas, H. Muazu, T. A. Zarma y A. Galadima, “Finite element analysis of EMAT using COMSOL *Multiphysics*,” in *Proc. Int. Conf. Electronics, Computer and Computation (ICECCO)*, 2017, doi: 10.1109/ICECCO.2017.8333338.

[8] G.-F. Zhai, W.-B. Jia, B. Liang, J.-X. Yang y C. Li, “EMAT phased array system for plate inspection,” in *Proc. Far East NDT New Technology & Application Forum (FENDT)*, 2017, pp. 40–44, doi: 10.1109/FENDT.2017.8584609.

[9] X. Guo, W. Zhu, X. Qiu y Y. Xiang, "A Lorentz force EMAT design with racetrack coil and periodic permanent magnets for selective enhancement of ultrasonic Lamb wave generation," *Sensors*, 2023, art. no., doi: 10.3390/s23010096.

[10] J. Lan, J. Zhang, X. Jia y R. Gao, "Optimization design of surface wave electromagnetic acoustic transducers based on simulation analysis and orthogonal test method," *Sensors*, 2022, art. no., doi: 10.3390/s22020524.

[11] D. Wu et al., "Design optimization of coil-only electromagnetic acoustic transducers and their detection circuits for stainless steel 304," *Russian Journal of Nondestructive Testing*, 2025, art. no., doi: 10.1134/S1061830925603551.

[12] Y. Li, Z. Liu, Y. Zheng, X. Guo, W. Yuan, y P. Zhao, "Transverse crack detection of rail base considering wedge-like structure and using a bulk-wave electromagnetic acoustic transducer," *IEEE Trans. Instrum. Meas.*, vol. 71, pp. 1–9, 2022, doi: 10.1109/TIM.2022.3154809.

[13] C. Wang, J. Ma, X. Bai, y J. Chen, "Defect detection and imaging using electromagnetic acoustic transducer with butterfly coil," *Review of Scientific Instruments*, vol. 95, 2024, doi: 10.1063/5.0198404.

[14] A. K. Gautam, C. C. Yin, y B. Bhattacharya, "Enhancing shear horizontal wave generation with a multilayer coil electromagnetic acoustic transducer," *IEEE Trans. Instrum. Meas.*, vol. 73, pp. 1–8, 2024, doi: 10.1109/TIM.2024.3476617.

[15] Z. Lv, W. Guan, Y. Zhang, W. Li, y M. Que, "An innovative meander line coil-based electromagnetic acoustic transducer for single-mode Lamb wave excitation," *Sensors and Actuators A: Physical*, vol. 399, art. 117445, 2026, doi: 10.1016/j.sna.2025.117445.

[16] L. Du, R. Gao y X. Jia, "Antisymmetric Lamb wave simulation study based on electromagnetic acoustic transducer with periodic permanent magnets," *Sensors*, vol. 23, art. 7117, 2023, doi: 10.3390/s23167117.

[17] V. A. Strizhak y A. V. Pryakhin, "Optimization of the parameters of the magnetizing device of the electromagnetic-acoustic transducer," *Devices and Methods of Measurements*, vol. 14, pp. 81–95, 2023, doi: 10.21122/2220-9506-2023-14-2-81-95.

[18] B. Liang, Z. Li, W. Tao, Q. Wang, Y. Yu y G. Zhai, "Giant magneto-acoustic transduction efficiency of a novel magnetostrictive-based electromagnetic acoustic transducer," *Measurement*, vol. 246, art. 116720, 2025, doi: 10.1016/j.measurement.2025.116720.

[19] L. Xiang, S. Dixon, C. B. Thring, Z. Li y R. S. Edwards, "Lift-off performance of electromagnetic acoustic transducers (EMATs) for surface acoustic wave generation," *NDT & E International*, vol. 126, art. 102576, 2022, doi: 10.1016/j.ndteint.2021.102576.

[20] X. Zhang, W. Li, B. Li, J. Tu, C. Liao, Q. Wu, S. Feng y X. Song, "A new design of the dual-mode and pure longitudinal EMAT by using a radial-flux-focusing magnet," *Sensors*, vol. 22, art. 1316, 2022, doi: 10.3390/s22041316.